Three dimensional characterisation of chromatography bead internal structure using X-ray computed tomography and focused ion beam microscopy

T.F. Johnson [a], J.J. Bailey [b], F. Iacoviello [b], J.H. Welsh [c], P.R. Levison [c], P.R. Shearing [b], D.G. Bracewell [a],*

[a] Department of Biochemical Engineering, University College London, Bernard Katz, London, WC1E 6BT, United Kingdom
[b] Electrochemical Innovation Lab, Department of Chemical Engineering, University College London, Torrington Place, London, WC1E 7JE, United Kingdom
[c] Pall Biotech, 5 Harbourgate Business Park, Southampton Road, Portsmouth, PO6 4BQ United Kingdom

ARTICLE INFO

ABSTRACT

X-ray computed tomography (CT) and focused ion beam (FIB) microscopy were used to generate three dimensional representations of chromatography beads for quantitative analysis of important physical characteristics including tortuosity factor. Critical-point dried agarose, cellulose and ceramic beads were examined using both methods before digital reconstruction and geometry based analysis for comparison between techniques and materials examined.

X-ray 'nano' CT attained a pixel size of 63 nm and 32 nm for respective large field of view and high resolution modes. FIB improved upon this to a 15 nm pixel size for the more rigid ceramic beads but required compromises for the softer agarose and cellulose materials, especially during physical sectioning that was not required for X-ray CT. Digital processing of raw slices was performed using software to produce 3D representations of bead geometry.

Porosity, tortuosity factor, surface area to volume ratio and pore diameter were evaluated for each technique and material, with overall averaged simulated tortuosity factors of 1.36, 1.37 and 1.51 for agarose, cellulose and ceramic volumes respectively. Results were compared to existing literature values acquired using established imaging and non-imaging techniques to demonstrate the capability of tomographic approaches used here.

1. Introduction

Liquid chromatography systems consist of porous, microspherical beads [1] that are packed into a cylindrical column [2], with the three dimensional structure of both the packed beds and individual beads being important to key performance metrics [3]. The surface area of a chromatography bead is maximised by having an internal structure comprised of intricate pore networks [4–6], with various materials of construction used as the backbone [1] for size exclusion or chemical based separation processes [7].

Chromatography beads have previously been characterised for several important aspects [8] such as porosity and tortuosity [9] in addition to performance based metrics [10,11]. Both imaging and non-imaging approaches have been used [8,12], with Inverse Size Exclusion Chromatography (ISEC) being commonly used to determine internal pore sizes [13]. Another available method for pore size investigations is mercury porosimetry [12] which is also used for porosity calculations. Tortuosity has been relatively more difficult to define for internal chromatography bead structures, particularly using imaging techniques, however methods such as using Bruggeman relationships, dilution methods [14] and other equation based approaches have been the most common methods for doing so.

Two main imaging approaches have been extensively used for both visualisation and quantification of chromatography bead structure: confocal laser scanning microscopy (CLSM) [14–16] and electron microscopy [8]. CLSM has been demonstrated to be capable of imaging the internal structure of a chromatography bead without the need for physical sectioning, however CLSM lacks the resolution capabilities for defining internal bead pores [3,11,17,18],

X-ray computed tomography - Zeiss Xradia 810 Ultra
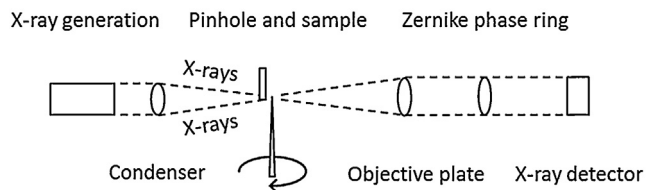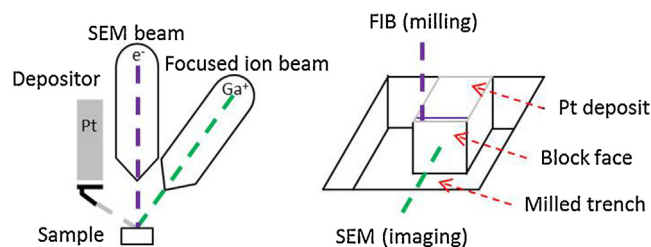

Focused ion beam – Zeiss XB1450 'Crossbeam'

Fig. 1. Schematics for X-ray computed tomography and focused ion beam systems. For X-ray computed tomography, emitted X-rays are directed towards the bead on top of the pin before detection, with projections subsequently reconstructed into a three dimensional volume. For focused ion beam microscopy, a sample is aligned between milling and imaging beams (left) before sample preparation, where an internal bead volume is isolated by milling a trench (right) over a platinum covered bead. An exposed block face within the bead is imaged before sequential 'slice and view' to produce a series of 2D electron micrographs.

whilst electron microscopy can display the detailed porous structure at the surface but has no natural sample penetration beyond thin sliced samples [6,10,16].

This has made both visualisation and subsequent quantification of the entire chromatography bead detailed microstructure difficult using existing imaging approaches as these techniques either lack sufficient resolution or internal structure visualisation, requiring a method to physically cut through bead material for nano-scale imaging. Microtomy has been demonstrated in other studies to be capable of cutting through chromatography resins [8]. However producing a series of thin nano-slices for the softer chromatography materials resulted in microtomy being excluded from this study; although use of approaches such as serial block face microtomy [19] may be a more viable alternative for successfully applying microtomy to beads.

While parameters such as porosity have been extensively characterised for a wide array of industrially relevant resins using non-imaging techniques [4,8,9], tortuosity has been a point of contention in terms of the most representative method of evaluation in addition to the actual range of tortuosity for chromatography resins. From 1.3 to 6 [9,14,19] across various types, this presents a vast difference in estimation of tortuosity that influences key performance metrics such as transfer and diffusivity within a chromatography bead [9,20].

Therefore, imaging approaches for visualisation and quantification of internal chromatography bead structure are presented here, achieving resolution superior to CLSM whilst enabling subsurface imaging not available when using conventional electron microscopy [21]. The issue of penetrating material whilst attaining a sufficient pixel size and quality was the main criteria for technique selection and optimisation, with X-ray Computed Tomography (CT) and Focused Ion Beam (FIB) microscopy selected to image agarose, cellulose and ceramic beads. Tomographic imaging has been used in other fields to provide a method for simulating tortuosity factor [21–24] where, like in chromatography studies, the methods used

have typically relied on empirical or equation based derivations [9,19,25].

In a previous study [26], X-ray CT was used to investigate packed bed *inter*-bead structure of cellulose and ceramic based columns, although the pixel size and field of view requirements were of different scales [1]. X-ray 'nano-CT' [26–28] has been used to represent other porous structures and so was deemed appropriate to image and reconstruct the 3D internal structure of conventional chromatography beads, albeit of different materials to those investigated here.

Focused ion beam microscopy [29,30] was also used, a technique that relies on milling via a gallium ion beam and then sample imaging using electron microscopy to generate a sequence of two dimensional images; which can be reconstructed into a 3D structure or to produce samples for TEM or X-ray CT [27,31,32]. Fig. 1 displays overall schematics for X-ray CT and FIB imaging used to provide the basis for 3D bead structural representation.

Each technique has relative advantages and disadvantages [21,27,32,33], but provide distinctly different methods of producing 3D structures at high resolutions; both in terms of pixel sizes achievable as well as the approach required in order to obtain tomographic data-sets of sufficient quality for visualisation and quantification of structural geometry.

Using two different tomographic approaches for 3D bead visualisation and quantification enabled comparisons both between results obtained for each bead type and overall technique suitability. Important considerations for determining the capability for using tomographic approaches for visualisation and quantification of bead internal structure included accuracy of results when compared to established literature techniques, in addition to general ease-of-use and feasibility for applying 3D imaging to relevant chromatography beads of different materials.

Consideration included both the quantifiable results obtained after imaging and processing in addition to requirements for imaging using X-ray CT and FIB. Porosity, tortuosity factor, surface area to volume ratio and pore size of each sample are discussed in relation to the technique used and material examined in addition to identifying relevant advantages and disadvantages of using X-ray CT and FIB microscopy for bead visualisation and evaluation.

Comparisons to values obtained using established techniques would enable determination of X-ray CT and FIB microscopy suitability for visualising and characterising the 3D structure of chromatography beads. Tortuosity evaluation of the internal pore network in particular was of interest given the relative difficulty in accurately measuring this aspect, despite its importance in relation to mobile phase flow paths through internal bead structure.

2. Materials and methods

2.1. Chromatography bead source

Agarose beads used in this study were Capto Adhere resin from GE Life Sciences (Uppsala, Sweden). Cellulose and ceramic materials were provided by Pall Biotech (Portsmouth, United Kingdom) in the form of CM Ceramic HyperD™ F or MEP HyperCel™ 100 mL sorbent containers in 20% ethanol storage buffers before drying processes were performed in parallel. Investigations were performed in parallel for each bead type and so are referred to as sample or beads collectively. Average bead diameters for agarose, cellulose and ceramic beads were found to be 70 μm, 86 μm and 53 μm respectively based on optical imaging of a small sample as a reference on size, with whole bead X-ray slices available in Fig. 2.

Table 1
Requirements and outputs for each tomography based technique used. Dimensions stated are total overall volumes analysed, with sub-volumes also generated in each case for analysis purposes.

Technique	Preparation	Methods	Pixel size (nm)
X-ray computed tomography	Critical-point drying, pinhead adhesion	LFOV, Adjusted	63
		High resolution	32
Focused ion beam microscopy	Drying, embedding, coating, milling	Slice and view	15 – 40

2.2. Sample preparation

Initial sample preparation was performed by dehydrating each material type to a 100% ethanol concentration from the original 20% as a requirement for drying. Subsequent critical-point drying [34] was performed using a Gatan critical-point dryer to displace ethanol with carbon dioxide as performed by Nweke et al [35]. on beads.

After critical-point drying, samples were sub-divided for X-ray computed tomography and focused ion beam microscopy, which required further preparation. For X-ray CT samples, an individual bead was isolated and held in place on top of a sharp pin using contact adhesive and stored in a sealed container for 24 h before use to ensure that the bead had been correctly set in place before scanning.

For FIB preparation, approximately 100 of each bead type were inserted into a Struers (Westlake, Ohio, United States) 25 mm mould, with a brass subdivide used in order to separate and isolate agarose, cellulose and ceramic samples. EpoFix (Struers) epoxy and hardener mixture were added to fill the mould in 15:2 parts respectively, before vacuum desiccation of the sample for 24 h to remove trapped air from the sample.

The embedded puck was then removed from the desiccator for smoothing of the sample surface to expose beads using silicon carbide sheets (Agar Scientific, Stansted, United Kingdom) of increasing grit rating: 360, 600, 1,200, 2400 and finally 4000 before diamond paste polishing; finishing with gold coating using an Agar Scientific coater performed to increase sample conductivity and reduce charging. Prepared samples were adhered to a 25 mm aluminium stub using conductive Leit C cement (Agar Scientific, United Kingdom) with a silver bridge added in order to ensure conductivity between the sample and stub.

2.3. X-ray computed tomography

A pin-mounted bead was placed in a Zeiss Xradia 810 Ultra (Pleasanton, California, United States) at the Electrochemical Innovation Laboratory in UCL at an accelerating voltage of 35 kV used in each case using a chromium target. The sample was rotated through 180° during imaging. Large Field Of View (LFOV) mode was used to image the entire bead achieving a 63 nm pixel size. This was improved to 32 nm using High Resolution (HRES) mode by applying binning mode 2 on a 16 nm original pixel size; however this compromised the field of view to the top 16 μm of the sample, of which further cropping was often required.

2.4. Focused ion beam

Stub-mounted samples were inserted into a Zeiss XB1540 'Crossbeam', with an accelerating voltage of 1 kV used in secondary electron detection mode for imaging with the stage tilted to 54° for crossbeam alignment. After selecting a suitable bead, 500 nm thick platinum deposition was performed over the area of interest in order to provide a smooth protective surface for precise milling over the internal bead volume to be subsequently imaged.

A preparatory trench at a depth of approximately 30 μm was milled using the gallium ion beam at a current of 1 nA in order to expose the protrusion capped by deposited platinum with block face polishing performed at 200 pA. Subsequent 'slice and view' imaging and milling at 100 pA of the block face at set intervals was used to generate a series of JPEG images for each sample. For ceramic results, a cubic voxel size of 15 nm was used, whilst for agarose and cellulose beads 20 nm width and height at a depth of 40 nm was achieved in both cases. A Helios NanoLab 600 was used instead for cellulose beads as a replacement system, however the approach taken was in-line with settings used for the other samples.

2.5. Image processing

As with image processing performed in a previous study [26], either 2D images or 3D TXM files were loaded into Avizo® (FEI, Bordeaux, France). For FIB microscopy image sequences, the StackReg plugin for ImageJ [36] was used to align all slices correctly before insertion into Avizo for processing and analytical purposes [37–39]. The main objective of the processing stages was to produce an accurate representation of internal bead structure by segmenting material and void phases in addition to artefact removal.

For X-ray CT samples the same bead was used for LFOV and HRES imaging, where extraction of a sub-volume at the relevant coordinates enabled generation of a LFOV volume in the same position as the HRES counterpart for comparison purposes, with this new volume referred to as 'adjusted' or 'ADJ' with Table 1 displaying approaches used. Analysis of geometric porosity, geometric tortuosity, available surface area to volume ratio and average pore diameter were calculated within Avizo, with tortuosity factor in each case determined using the MATLAB® plugin *TauFactor* [23] by using 3D TIFF files.

3. Results and discussion

3.1. X-ray computed tomography

To evaluate the porous structure in an individual chromatography bead using X-ray CT, two different modes were used considering the trade-off between optimising pixel size and total sample imaged. This was performed to determine the impact of improving pixel size on both the capability for X-ray CT to accurately visualise the intricate structure of the bead in addition to quantify parameters such as porosity and tortuosity. Fig. 2 displays slices of cellulose and ceramic bead samples using LFOV and HRES approaches using the best available cubic voxel size in each case having respective dimensions of 63 nm and 32 nm.

It was observed that all 2D slices in Fig. 2 display an internal porous structure for agarose, cellulose and ceramic beads, with the characteristic shell visible around the ceramic sample. Large voids were observed to occur for all materials within the internal structure of the samples which was also visible in microtome slices presented by Angelo et al. [8] for cellulose beads, which would have been difficult to find without the use of 3D imaging techniques, with penetration of the adherent epoxy also obscuring some structure.

The high resolution images were found to visualise a more intricate porous structure with smaller features relative to the large field of view counterparts, which was particularly noticeable for cellu-
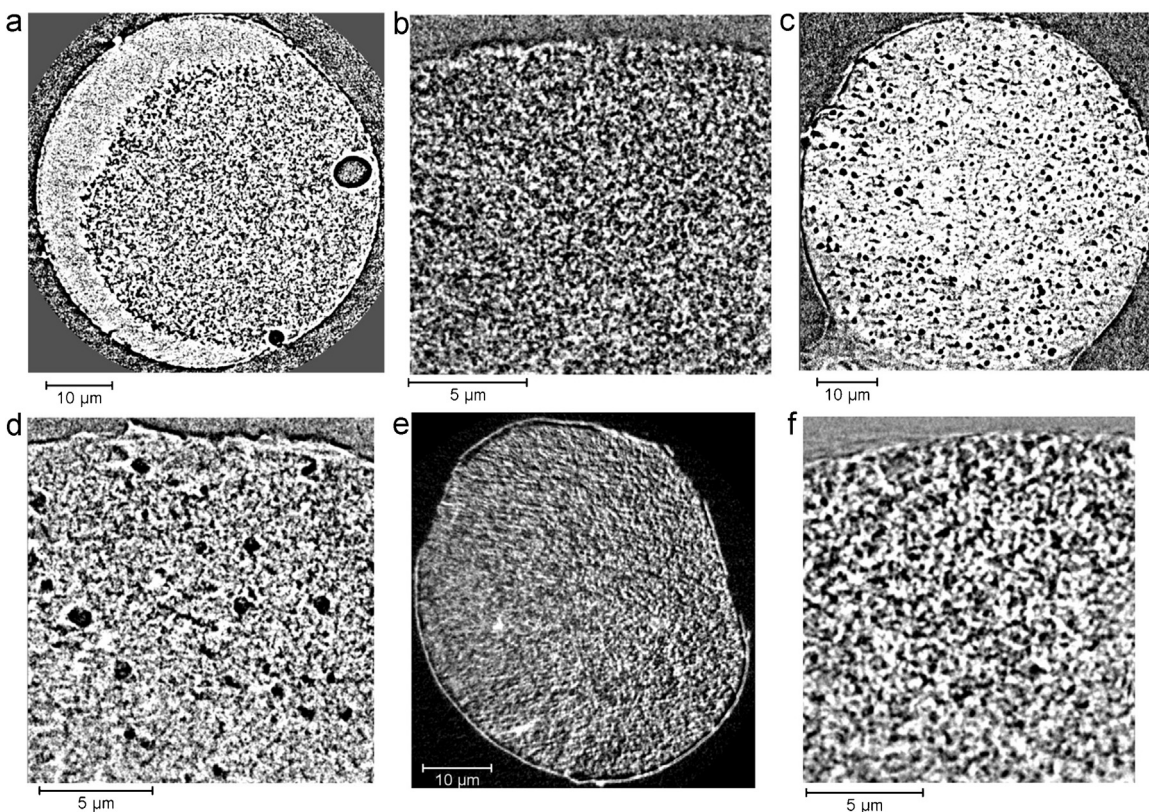
Fig. 2. Chromatography bead imaging using X-ray computed tomography. **A**: Agarose bead imaged in large field of view mode. **B**: Agarose bead imaged in high resolution mode. **C**: Cellulose bead imaged in large field of view mode. **D**: Cellulose bead imaged in high resolution mode. **E**: Ceramic bead imaged in large field of view mode. **F**: Ceramic bead imaged in high resolution mode.

lose samples due to the larger pores that were visible at both scales, but with high resolution images also displaying smaller surrounding pore networks.

This indicated that improving the pixel size from 63 nm to 32 nm enabled a greater degree of chromatography bead internal structure identification and thus would be considered to be more representative of the porous geometry within each bead, particularly for agarose and cellulose slices. However, using HRES mode also limited the field of view to the top of the bead in each case, pre-

venting analysis of the entire sphere using this approach, requiring a sub-volume LFOV imaging to be produced in order to provide direct comparison between pixel sizes at the same coordinates for each of the materials investigated.

X-ray CT was demonstrated to be capable of imaging the 3D porous structure of various chromatography materials without having to physically section the beads. This also enabled multiple acquisitions of the same volume without destroying the sample for optimisation purposes and comparisons between the resolu-
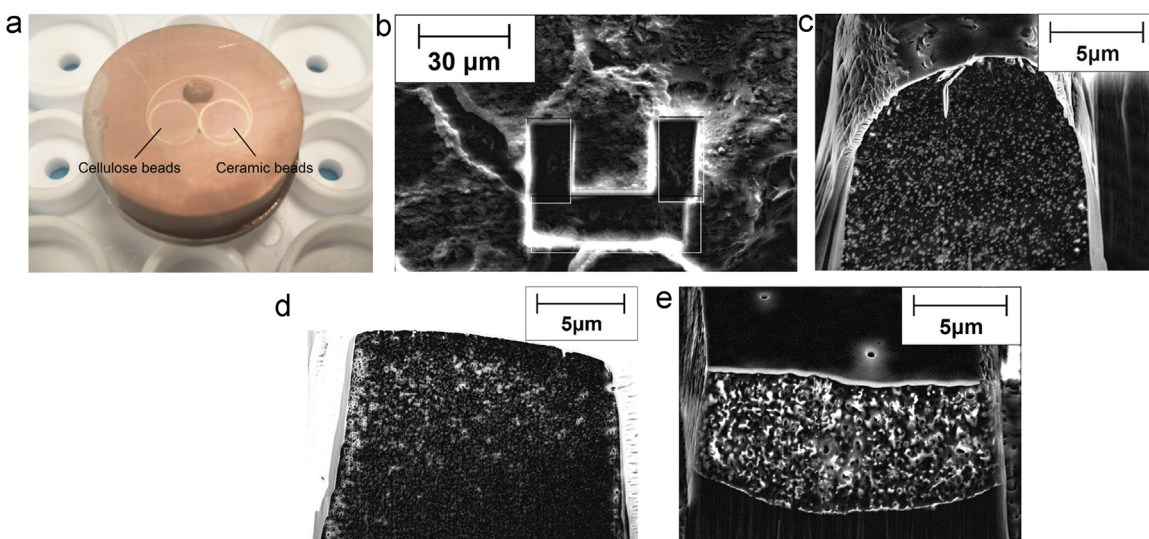

Fig. 3. Focused ion beam microscopy of chromatography beads. **A**: Coated sample puck with two bead types. **B**: 'Overhead' FIB view of a milled trench. **C**: Agarose block face. **D**: Cellulose block face. **E**: Ceramic block face.
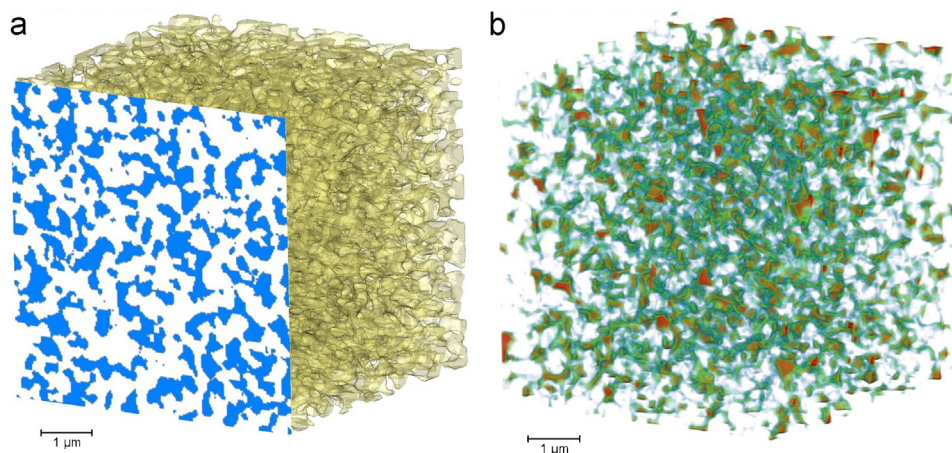
Fig. 4. Evaluation of cellulose bead 3D structure from a HRES scan. **A**: 2D slice overlaying a 3D render, blue and yellow – material, white – void. **B**: Porous distance map, green <100 nm from material, yellow < 200 nm, red > 200 nm (For interpretation of the references to colour in this figure legend, the reader is referred to the web version of this article).

tion and field of view. The main disadvantage of using X-ray CT was the pixel size available because even when achieving 32 nm in HRES mode, alternative techniques such as ISEC used on similar materials [8] suggest that the finest structure may not have been identified due the pore sizes being smaller than pixel dimensions achieved by X-ray CT and FIB imaging, requiring a higher resolution 3D approach.

3.2. Focused ion beam microscopy

FIB has previously been used as a basis for analysing porous materials, analogous to chromatography bead internal structure, and so was selected to achieve an improved pixel size relative to X-ray CT due to the differences observed between resolution and field of view images. The difference in pixel size dimensions between X-ray CT modes was approximately 2, therefore this approach was kept constant for higher resolution FIB imaging by achieving pixel size dimensions of 15 nm. Cubic voxels were preferred despite potential further pixel size gains available using FIB, however this would compromise the overall volume that could be imaged for each sample and would present further imaging issues.

Whilst a 15 nm pixel size was achieved for ceramic imaging, the softer agarose and cellulose displayed stability issues and so required a reduction in both block face pixel size to 20 nm in addition to slice depth being increased to 40 nm. This was undesirable in terms of both losing pixel size as well as preventing direct parity across all FIB volumes in terms of voxel dimensions; however was a necessary compromise for stable slice-and-view.

Important considerations involved with sample preparation before imaging included ensuring that as much air was removed from the sample during epoxy embedding as possible in order to minimise disruptions to the continuous epoxy phase. Imaging difficulties at this stage would require artefact removal during digital processing in addition to potentially compromising milling quality in the local area by causing issues such as streaking effects [32]. Fig. 3 displays a sample puck containing 2 different bead types, an overhead view of a bead after trench milling and block face slices for the agarose, cellulose and ceramic beads.

It was observed in Fig. 3 that structure can be identified embedded within the epoxy for all materials, with again the characteristic shell visible for the ceramic bead visible as was the case for X-ray CT imaging. Platinum deposition that formed a smooth surface on the top sample can be seen that was used to increase conductivity in addition to reducing streaking artefacts that distort the block face in each slice, with the epoxy impregnation performed under

vacuum to minimise air pockets. Whilst artefact reduction before reconstruction was successful, some instances still occurred and required digital correction afterwards.

3.3. Comparison between X-ray CT and FIB

Both techniques have been demonstrated to be capable of producing visual representations of agarose, cellulose and ceramic chromatography bead structure, although each technique had relative advantages and disadvantages. The main advantage of FIB compared to X-ray CT was that the pixel size achievable was superior to either X-ray CT mode, potentially enabling smaller features in the structure to be identified which would result in more accurate measurements of characteristics such as porosity and pore sizes compared to ISEC etc.

However, a FIB approach did have several drawbacks, including being a destructive technique, which meant that the sample could only be imaged once unlike for X-ray CT where the same bead could be examined multiple times, enabling comparative optimisation [26]. The second disadvantage to using FIB was the increased sample preparation requirements, which could result in undesirable changes to the sample itself [8], with the epoxy puck inherently susceptible to air pockets and streaking artefacts that were minimised but not eliminated entirely. X-ray CT was also capable of imaging the entire bead whilst using a FIB approach limited the overall volume that could be prepared and then milled.

Overall, the superior pixel size achieved by FIB was countered by various attributes that make X-ray CT relatively more convenient to use whilst still being able to resolve chromatography bead internal structure. This highlights that suitable technique selection relies on various factors that need to be considered in relation to the sample itself and the final imaging requirements, of particular interest being the pixel size achievable in relation to expected feature sizes. Both techniques performed considerably better for ceramic beads compared to the softer agarose and cellulose samples, as stability issues were encountered using FIB and X-ray CT imaging in particular for agarose and cellulose beads.

3.4. Tomographic analysis

The reconstructed volumes were processed in Avizo in order to segment the bead and void phases, in addition to removing any artefacts that had occurred due to sample preparation or imaging. Digitally processed geometries were then analysed for porosity, tortuosity factor, surface area to volume ratio and average pore

Table 2

Results from tomography based analysis of bead volumes. Average values are presented in each case, with X-ray computed tomography – Adjusted being the same volume as the reduced field of view results but taken from the large field of view data-set for comparison. Results are reported to three significant figures, with one standard deviation displayed below the mean value. Surface area to volume ratio is normalised against the lowest average.

	Edge			Centre		
	Top	Middle	Bottom	Top	Middle	Bottom
Agarose						
Geometric porosity (%)	**34.5**	**32.0**	**31.5**	**39.3**	**36.2**	**33.0**
	± 0.3	± 1.5	± 0.6	± 2.7	± 2.5	± 0.9
Geometric tortuosity	**1.33**	**1.35**	**1.45**	**1.32**	**1.38**	**1.39**
	± 0.02	± 0.02	± 0.02	± 0.02	± 0.04	± 0.02
Surface area to volume ratio	**0.103**	**0.099**	**0.150**	**0.105**	**0.104**	**0.152**
	± 0.009	± 0.005	± 0.001	± 0.011	± 0.005	± 0.005
Average pore diameter (μm)	**20.6**	**21.1**	**19.2**	**18.7**	**21.1**	**19.9**
	± 1.8	± 1.6	± 0.5	± 1.2	± 0.9	± 0.4
Cellulose						
Geometric porosity (%)	**34.2**	**32.3**	**36.9**	**37.0**	**38.6**	**37.6**
	±0.4	±2.0	±0.7	±3.3	±0.4	±0.7
Geometric tortuosity	**1.81**	**1.77**	**1.59**	**1.79**	**1.79**	**1.62**
	±0.04	±0.05	±0.02	±0.06	±0.02	±0.08
Surface area to volume ratio	**0.126**	**0.094**	**0.110**	**0.121**	**0.113**	**0.115**
	±0.003	±0.007	±0.001	±0.002	±0.001	±0.008
Average pore diameter (μm)	**10.0**	**10.2**	**9.4**	**10.0**	**11.1**	**9.0**
	±0.1	±0.2	±0.2	±0.2	±0.1	±0.7
Ceramic						
Geometric porosity (%)	**32.6**	**32.7**	**30.0**	**36.9**	**36.1**	**35.4**
	±0.8	±0.8	±0.6	±1.5	±0.9	±1.0
Geometric tortuosity	**1.47**	**1.40**	**1.42**	**1.39**	**1.34**	**1.36**
	±0.03	±0.02	±0.03	±0.02	±0.02	±0.03
Surface area to volume ratio	**0.091**	**0.100**	**0.083**	**0.100**	**0.106**	**0.094**
	±0.002	±0.003	±0.002	±0.004	±0.001	±0.003
Average pore diameter (μm)	**10.7**	**10.6**	**11.0**	**11.7**	**10.9**	**12.1**
	±0.2	±0.1	±0.2	±0.4	±0.1	±0.4

diameter. For X-ray CT LFOV samples, cubic volumes of 40 μm dimensions were analysed, whilst for HRES and FIB volumes dimensions of 10 μm–15 μm were obtained for structural quantification. Using a 3D approach enabled visualisation of key aspects relating to chromatographic structure, with Fig. 4 displaying outputs based on cellulose HRES X-ray CT imaging.

Producing 3D representations of chromatography bead structure enabled visualisation of important geometric aspects such as void-distance maps to aid understanding of chromatography bead structure and pore geometry, with Fig. 5 showing results for porosity and pore size across the different materials and approaches used. To provide direct comparison between LFOV and HRES X-ray CT imaging for each bead, a sub-volume with identical co-ordinates was produced with the difference being pixel size achieved in each case. This was referred to as the 'adjusted' volume, or 'ADJ.'

It was observed that X-ray CT porosity readings from Fig. 5 for each material were similar between 63 nm and 32 nm pixel size approaches used, with agarose and cellulose close to 70% in each case and ceramic 65%. Ceramic beads of the same HyperD family have previously been determined to have an average porosity of 61% using Maxwell derived equations based upon cross sectional area available [14] suggesting that tomographic representation was accurately determining porosity values for the overall ceramic structure.

However, for agarose and cellulose beads porosity readings are typically reported in the 80%–90% range using a variety of established techniques such as ISEC on popular and commercially available resins, although porosities down to below 70% have been reported [1,4,40]. Therefore whilst the average porosities presented here lie within these ranges, the tomographic approaches displayed a considerably lower porosity to those values typically observed, albeit dependent on variation between different types of agarose and cellulose beads available. By using an improved average pixel size via a focused ion beam slice and view approach between 15 nm

and 25 nm, increased porosities closer to 80% were observed that were closer to expected values suggested by other methods such as ISEC [14].

Whilst similarities in results were observed for overall bead porosity between imaging techniques, clear disparities were apparent when evaluating average pore sizes. In all cases, the 63 nm X-ray CT volumes were found to have a much larger average pore size compared to the high resolution and FIB counterparts, despite the similar overall porosities. This was attributed to the inferior pixel size being unable to discern the finest chromatography bead structural features, supported by relative surface area to volume ratios displayed in Table 2 being considerably higher for the improved resolution approaches.

Average pore sizes suggested in literature using established techniques cover a vast range for relevant bead materials, from below 10 nm determined using ISEC [8] up to 100 nm [1], suggesting the difficulty in accurately determining pore size. Whilst the large field of view and adjusted counterparts displayed results above 130 nm in all cases, the higher resolution approaches suggested values between 60 nm and 100 nm across each material which was within the expected range and order of magnitude, albeit at the higher values [1,4,8]. Angelo et al. [8] does discuss the potential for SEM imaging for pore size determination of cellulose beads to result in an approximate average of 50 nm on the surface.

Differences were expected between tomographic imaging methods when determining average pore size due to the differing pixel dimensions, where the minimum theoretical pore size would be 1 pixel. By obtaining an improved pixel size, finer porous network could be resolved as can be seen in Fig. 2 when comparing LFOV and HRES X-ray CT visualisation of chromatography bead structure. Whilst ceramic results displayed a decreasing average pore size upon improving average voxel size, agarose and cellulose counterparts have the smallest average pore size determine by X-ray CT. This was attributed to despite having a superior average
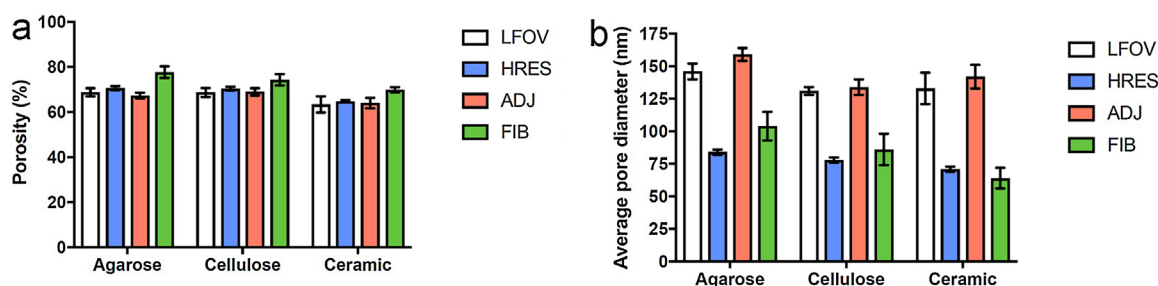
Fig. 5. Porosity readings for X-ray CT and FIB imaged volumes. **A**: Porosity. **B**: Average pore diameter.

voxel dimensions of 25 nm–32 nm, by compromising to a 40 nm slice thickness the smallest pore structure obtainable was reduced for softer bead materials.

Overall, tomographic quantification demonstrated that for aspects such as average pore size evaluation, achieving the best pixel size possible was favourable to obtain more representative results by using either high resolution X-ray CT or FIB. However, for overall porosity measurements there was no major difference between X-ray CT imaging of the same bead even at different pixel sizes. This suggested that the technique used for tomographic imaging should also be based upon the desired outcomes, as using higher resolution methods can include required compromises such as field of view loss.

Whilst aspects such as porosity are relatively straightforward to characterise using existing non-imaging methods for chromatography beads, others such as tortuosity have been both ill-defined and quantified despite the inherent importance to liquid flow paths and thus transfer between phases [9,14]. Using a tomographic approach in other fields has been found to be an effective way to evaluate tortuosity, with continued efforts to standardise and better represent this factor [23]. Therefore two methods were selected for this study: geometric tortuosity and tortuosity factor based upon the 3D volumes produced from imaging. The geometric variant was determined by relating the average path length through a segmented porous volume to the shortest distance possible being commonplace [24,41].

Tortuosity factor was evaluated using *TauFactor* software that considers simulated steady state diffusion through the tomographic structure that is compatible with existing fundamental relationships [23]. This enabled a more complex evaluation of tortuosity compared to geometric tortuosity which relies on slice-to-slice positional movement without consideration of geometry-based flux constrictions. Results for both geometric tortuosity and tortuosity factor variants are displayed in Fig. 6.

Tortuosity results for both measurement approaches were found to be below 2, which was at the lower end of the range as reported by 6 other studies into tortuosity of chromatography beads using other methods [9,14]. A highly porous structure reconstructed from tomographic imaging as was obtained in each case here would result in low tortuosity readings, however the method for determining tortuosity is a major factor to consider [24], particularly given the relatively lower porosities here compared to other methods. As expected, tortuosity factor was found to be greater than geometric counterparts for all materials and tomographic methods, with an average difference of 0.22 for softer agarose and cellulose volumes and 0.07 for ceramic counterparts.

This was attributed to tortuosity factor considering neighbouring pixels of the same phase, which allows for a greater appreciation of an increased tortuosity in regions with finer pore sizes that are less represented when evaluating geometric tortuosity that relies upon a scalar flow through pores regardless of size and is solely impacted by relative void position and slice-to-slice movement.

However, inconsistencies between Avizo and TauFactor results have been documented by Cooper et al. [23] and so may be a contributing factor here.

A major advantage of using a tomographic approach for 3D imaging and reconstruction for visualisation of chromatography bead internal structure was that the digital volume could be quantitatively analysed for various important geometric characteristics. This also enabled comparison of results to those obtained in literature using established techniques that have either relied on alternative imaging techniques or non-imaging methods including ISEC, BET and mercury porosimetry, which have been compared for porosity, tortuosity and average pore sizes in Table 3.

This suggested that further improvements to pixel size would endeavour in improving pore size determination accuracy for tomographic techniques when considering conventional chromatography beads, however the soft materials commonly used for resins provided issues that required compromises to aspects such as resolution to obtain stable imaging.

Achieving an optimal or relevant pixel size relies on knowing the smallest feature sizes in the structure [42] and is important for producing truly accurate representations of 3D structure at sufficient resolution, particularly if aspects such as average pore size are to be investigated that heavily rely on being able to resolve even the smallest pores. However, these approaches have been found to require several compromises in order to obtain high quality 3D representations compared to large field of view X-ray CT scanning.

The first of these was field of view, where an entire bead could be imaged when using X-ray CT at a 63 nm pixel size, but for the high resolution counterpart, only the very top of the spherical sample could be imaged due to the field of view constraints. The most credible way to image an entire bead of approximately 50 μm in diameter would be to perform mosaic scans, where many data-sets are acquired using HRES mode and then digitally stitched together to produce an overall volume that could cover the entire bead volume whilst maintaining a 32 nm voxel size.

However, this approach was deemed to be impractical as this would require a vast amount of time to achieve this, particularly problematic for the agarose and cellulose beads that displayed stability issues when exposed to the X-ray beam for any considerable amount of time. Another problem with mosaic imaging at such high quality is that in order to image the very centre of the sphere, a considerable amount of surrounding material would obscure the beam, detrimentally impacting the signal-to-noise ratio of imaging and also presenting issues when accurately determining volume boundaries.

FIB lift-outs [32] for X-ray CT could be attempted in order to alleviate this issue, however bead-epoxy definition would be required and the overall process would be more intensive than imaging using FIB itself. Simulating tortuosity factor in different orientations for the volumes examined was not found to produce results of particular difference to each other and so pore structure was not observed to have major directional disparities for tortuosity, with distance
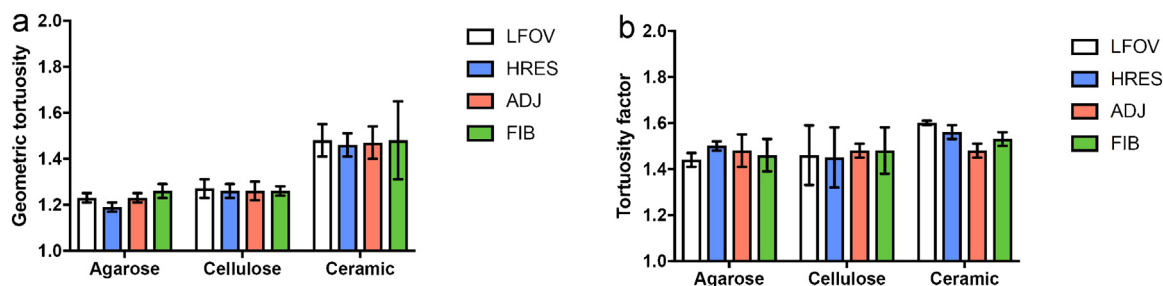
Fig. 6. Tortuosity readings of individual bead volumes. **A**: Geometric tortuosity. **B**: Tortuosity factor.

Table 3
Comparison of tomographic results of HRES X-ray CT to other methods. Tortuosity displayed for tomographic approaches is tortuosity factor. Overall bed porosity calculations for tomographic approaches are based upon *inter*-bead volume determined in a previous study [26] combined with overall bead porosity of the remaining stationary phase in each case, where column dimensions may not be identical in all cases. Different bead brands may have been joined under material groups [1,4,8,14,26].

	Methods	Porosity (%)	Tortuosity	Average pore size (nm)	Overall bed porosity (%)
Agarose					
Tomography	X-ray CT HRES	71	1.5	84	81
Barrande et al.	BET, Mercury porosimetry	87	1.32	37	92
Angelo et al.	ISEC			11.8 – 51.6	
DePhillips et al.	ISEC	84		49.4 – 54.6	90
Tatárová et al.	ISEC			28.8 – 109.8	
Cellulose					
Tomography	X-ray CT HRES	70	1.45	78	81
Barrande et al.	BET, Mercury porosimetry	90	1.3	19	91
Angelo et al.	ISEC, EM	66 – 74		8.8-10 (~50 for EM)	78 – 83
Tatárová et al.	ISEC			47.4	
Ceramic					
Tomography	X-ray CT HRES	65	1.56	71	77
Barrande et al.	BET, Mercury porosimetry	61	1.97	22	85
DePhillips et al.	ISEC	59 – 65		21 – 68	74 – 78

maps such as displayed in Fig. 4**B** useful for visualising chromatography bead structure. Tomographic approaches have also enabled consideration of pore geometry and morphologies, although the main value of interest here was average pore size for comparing to results obtained using ISEC and other approaches.

Table 3 displays comparisons of porosity, tortuosity and average pore sizes to existing literature values based upon established methods, where BET has also been commonly used to evaluate available surface area of internal bead structure [14] that was investigated in relative terms between tomographic techniques here. ISEC has been used for all 3 bead materials to quantify porosities and pore sizes, where overall bed porosity that includes *inter*-bead voidage had been determined. This could be quantified using 3D imaging by combining porosities obtained here with values obtained in a previous study [26].

Aforementioned lower porosities obtained using the various tomographic approaches resulted in corresponding reduced overall column porosities, although the exact bed geometry in each study was not identical. Whilst pore sizes were typically higher compared to other methods such as ISEC and mercury porosimetry, the same order of magnitude was achieved and results were in-line with values reported when imaging bead surfaces using electron microscopy [8,35].

Overall, these results suggested that the pixel sizes used were suitable for imaging bead internal structure, however the higher resolution approach of X-ray CT and FIB were more appropriate for quantification of characteristics such as pore size due to their inherent sensitivity to the smallest features that suggest results closer to those suggested by orthogonal methods [8,9]. On the contrary, aspects such as tortuosity did not show a definitive or reliable change when using higher resolution approaches, suggesting that visually identifying major pore networks would be sufficient

to approximate a tortuosity factor for the material, without the necessity of achieving a pixel size to accurately image the smallest features that may present other imaging considerations and obstacles.

4. Conclusions

X-ray CT and FIB have been demonstrated to be effective methods for imaging the 3D internal structure of three chromatography bead materials, yielding quantitative results that are relatable to established approaches for measurement. Different pixel sizes achieved were compared both between and within tomographic techniques explored here that highlighted the benefits of using nano-scale resolution approaches to both visualise and evaluate bead structure, in addition to requirements for representative imaging. Limitations, particularly when considering the softer bead types, resulted in constraints and thus compromises that would result in a greater degree of the smallest porous structures being obscured. These trade-offs may be possible to overcome upon technology advancement.

Future areas of interest include expanding the technique and material portfolio, as well as investigating chromatography use and application based impacts on bead structure. This would be greatly enhanced by improvement in X-ray CT or FIB technology by either further improving pixel sizes attainable whilst reducing constraints; as well as the availability of new techniques or technologies that enable new approaches to obtaining high quality tomographic representations of chromatography beads, including the smallest feature sizes. This would provide greater insight of how bead structure relates to important geometric factors such as tortuosity.

Acknowledgements

Appendix A. Supplementary data

Supplementary material related to this article can be found, in the online version, at doi:https://doi.org/10.1016/j.chroma.2018.06.054.

References

[1] I. Tatárová, M. Gramblicka, M. Antosová, M. Polakovic, Characterization of pore structure of chromatographic adsorbents employed in separation of monoclonal antibodies using size-exclusion techniques, J. Chromatogr. A 1193 (June (1–2)) (2008) 129–135.

[2] D.E. Cherrak, G. Guiochon, Phenomenological study of the bed–wall friction in axially compressed packed chromatographic columns, J. Chromatogr. A 911 (March (2)) (2001) 147–166, http://dx.doi.org/10.1016/S0021-9673(01)00518-0.

[3] S. Gerontas, M.S. Shapiro, D.G. Bracewell, Chromatography modelling to describe protein adsorption at bead level, J. Chromatogr. A 1284 (April (52)) (2013) 44–52, http://dx.doi.org/10.1016/j.chroma.2013.01.102.

[4] P. DePhillips, A.M. Lenhoff, Pore size distributions of cation-exchange adsorbents determined by inverse size-exclusion chromatography, J. Chromatogr. A 883 (June (1–2)) (2000) 39–54, http://dx.doi.org/10.1016/S0021-9673(00)00420-9.

[5] K.-F. Du, M. Yan, Q.-Y. Wang, H. Song, Preparation and characterization of novel macroporous cellulose beads regenerated from ionic liquid for fast chromatography, J. Chromatogr. A 1217 (February (8)) (2010) 1298–1304, http://dx.doi.org/10.1016/j.chroma.2009.12.037.

[6] B.D. Bowes, H. Koku, K.J. Czymmek, A.M. Lenhoff, Protein adsorption and transport in dextran-modified ion-exchange media. I: adsorption, J. Chromatogr. A 1216 (November (45)) (2009) 7774–7784, http://dx.doi.org/10.1016/j.chroma.2009.09.014.

[7] T. Müller-Späth, G. Ströhlein, L. Aumann, H. Kornmann, P. Valax, L. Delegrange, E. Charbaut, G. Baer, a Lamproye, M. Jöhnck, M. Schulte, M. Morbidelli, Model simulation and experimental verification of a cation-exchange IgG capture step in batch and continuous chromatography, J. Chromatogr. A 1218 (August (31)) (2011) 5195–5204, http://dx.doi.org/10.1016/j.chroma.2011.05.103.

[8] J.M. Angelo, A. Cvetkovic, R. Gantier, A.M. Lenhoff, Characterization of cross-linked cellulosic ion-exchange adsorbents: 1. Structural properties, J. Chromatogr. A 1319 (December (2013) 46–56, http://dx.doi.org/10.1016/j.chroma.2013.10.003.

[9] V. Wernert, R. Bouchet, R. Denoyel, Impact of the solute exclusion on the bed longitudinal diffusion coefficient and particle intra-tortuosity determined by ISEC, J. Chromatogr. A 1325 (January (2014) 179–185, http://dx.doi.org/10.1016/j.chroma.2013.12.029.

[10] E.J. Close, J.R. Salm, T. Iskra, E. Sørensen, D.G. Bracewell, Fouling of an anion exchange chromatography operation in a monoclonal antibody process: visualization and kinetic studies, Biotechnol. Bioeng. 110 (September (9)) (2013) 2425–2435, http://dx.doi.org/10.1002/bit.24898.

[11] S.C. Siu, R. Boushaba, V. Topoyassakul, A. Graham, S. Choudhury, G. Moss, N.J. Titchener-Hooker, Visualising fouling of a chromatographic matrix using confocal scanning laser microscopy, Biotechnol. Bioeng. 95 (November (4)) (2006) 714–723, http://dx.doi.org/10.1002/bit.21028.

[12] Y. Yao, A.M. Lenhoff, Determination of pore size distributions of porous chromatographic adsorbents by inverse size-exclusion chromatography, J. Chromatogr. A 1037 (May (1–2)) (2004) 273–282, http://dx.doi.org/10.1016/j.chroma.2004.02.054.

[13] L. Hagel, M. Ostberg, T. Andersson, Apparent pore size distributions of chromatography media, J. Chromatogr. A 743 (1996) 33–42, http://dx.doi.org/10.1016/0021-9673(96)00130-6.

[14] M. Barrande, R. Bouchet, R. Denoyel, Tortuosity of porous particles, Anal. Chem. 79 (23) (2007) 9115–9121, http://dx.doi.org/10.1021/ac071377r.

[15] M.S. Shapiro, S.J. Haswell, G.J. Lye, D.G. Bracewell, Design and characterization of a microfluidic packed bed system for protein breakthrough and dynamic

[16] binding capacity determination, Biotechnol. Prog. (2009) 277–285, http://dx.doi.org/10.1021/bp.99.

[16] L.E. Blue, E.G. Franklin, J.M. Godinho, J.P. Grinias, K.M. Grinias, D.B. Lunn, S.M. Moore, Recent advances in capillary ultrahigh pressure liquid chromatography, J. Chromatogr. A 1523 (2017) 17–39, http://dx.doi.org/10.1016/j.chroma.2017.05.039.

[17] J. Jin, S. Chhatre, N.J. Titchener-Hooker, D.G. Bracewell, Evaluation of the impact of lipid fouling during the chromatographic purification of virus-like particles from saccharomyces cerevisiae, J. Chem. Technol. Biotechnol. 2009 (June 2009) (2009), http://dx.doi.org/10.1002/jctb.2290.

[18] M. Pathak, A.S. Rathore, Mechanistic understanding of fouling of protein a chromatography resin, J. Chromatogr. A 1459 (August) (2016) 78–88, http://dx.doi.org/10.1016/j.chroma.2016.06.084.

[19] W. Denk, H. Horstmann, Serial block-face scanning electron microscopy to reconstruct three-dimensional tissue nanostructure, PLoS Biol. 2 (November (11)) (2004), http://dx.doi.org/10.1371/journal.pbio.0020329.

[20] A. Kim, H. Chen, Diffusive tortuosity factor of solid cake layers: a random walk simulation approach, J. Membrane Science 279 (2006) 129–139, http://dx.doi.org/10.1016/j.memsci.2005.11.042.

[21] A. Zankel, J. Wagner, P. Poelt, Serial sectioning methods for 3D investigations in materials science, Micron 62 (July) (2014) 66–78.

[22] D. Kehrwald, P.R. Shearing, N.P. Brandon, P.K. Sinha, S.J. Harris, Local tortuosity inhomogeneities in a lithium Battery composite electrode, J. Electrochem. Soc. 158 (12) (2011) A1393, http://dx.doi.org/10.1149/2.079112jes.

[23] S.J. Cooper, A. Bertei, P.R. Shearing, J.A. Kilner, N.P. Brandon, TauFactor : an open-source application for calculating tortuosity factors from tomographic data, SoftwareX 5 (2016) 203–210, http://dx.doi.org/10.1016/j.softx.2016.09.002.

[24] B. Tjaden, S.J. Cooper, D.J. Brett, D. Kramer, P.R. Shearing, On the origin and application of the Bruggeman correlation for analysing transport phenomena in electrochemical systems, Curr. Opin. Chem. Eng. 12 (May) (2016) 44–51, http://dx.doi.org/10.1016/j.coche.2016.02.006.

[25] J.R. Izzo, A.S. Joshi, K.N. Grew, W.K.S. Chiu, A. Tkachuk, S.H. Wang, W. Yun, Nondestructive reconstruction and analysis of SOFC anodes using X-ray computed tomography at sub-50 nm Resolution, J. Electrochem. Soc. 155 (5) (2008) B504, http://dx.doi.org/10.1149/1.2895067.

[26] T.F. Johnson, P.R. Levison, P.R. Shearing, D.G. Bracewell, X-ray computed tomography of packed bed chromatography columns for three dimensional imaging and analysis, J. Chromatogr. A 1487 (January) (2017) 108–115, http://dx.doi.org/10.1016/j.chroma.2017.01.013.

[27] P.J. Withers, X-ray nanotomography, Mater. Today 10 (December (12)) (2007) 26–34, http://dx.doi.org/10.1016/S1369-7021(07)70305-X.

[28] P.R. Shearing, J. Gelb, N.P. Brandon, X-ray nano computerised tomography of SOFC electrodes using a focused ion beam sample-preparation technique, J. Eur. Ceram. Soc. 30 (June (8)) (2010) 1809–1814, http://dx.doi.org/10.1016/j.jeurceramsoc.2010.02.004.

[29] D. Attwood, Nanotomography comes of age, Nature 442 (August) (2006) 642–643, http://dx.doi.org/10.1038/442642b.

[30] S. Reyntjens, R. Puers, A review of focused ion beam applications in microsystem technology, J. Micromechanics Microengineering 11 (July (4)) (2001) 287–300, http://dx.doi.org/10.1088/0960-1317/11/4/301.

[31] J.J. Bailey, T.M.M. Heenan, D.P. Finegan, X. Lu, S.R. Daemi, F. Iacoviello, N.R. Backeberg, O.O. Taiwo, D.J.L. Brett, A. Atkinson, P.R. Shearing, Laser-preparation of geometrically optimised samples for X-ray nano-CT, J. Microsc. 267 (3) (2017) 384–396, http://dx.doi.org/10.1111/jmi.12577.

[32] P.R. Shearing, J. Golbert, R.J. Chater, N.P. Brandon, 3D reconstruction of SOFC anodes using a focused ion beam lift-out technique, Chem. Eng. Sci. 64 (September (17)) (2009) 3928–3933, http://dx.doi.org/10.1016/j.ces.2009.05.038.

[33] J. Baek, A.R. Pineda, N.J. Pelc, To bin or not to bin? The effect of CT system limiting resolution on noise and detectability, Phys. Med. Biol. 58 (March (5)) (2013) 1433–1446, http://dx.doi.org/10.1088/0031-9155/58/5/1433.

[34] D. Bray, Critical Point drying of biological specimens for scanning electron microscopy, Supercrit. Fluid. Methods Protoc. Methods Biotechnol. 13 (2000) 235–243, http://dx.doi.org/10.1385/1-59259-030-6:235.

[35] M.C. Nweke, M. Turmaine, R.G. Mccartney, D.G. Bracewell, Drying techniques for the visualisation of agarose-based chromatography media by scanning electron microscopy Drying techniques for the visualization of agarose-based chromatography media by scanning electron microscopy, Biotechnol. J. (March) (2017), http://dx.doi.org/10.1002/biot.201600583.

[36] M.D. Abràmoff, I. Hospitals, P.J. Magalhães, M. Abràmoff, Image processing with ImageJ, Biophotonics Int. 11 (7) (2004) 36–42, ISSN 1081-8693.

[37] F. Tariq, V. Yufit, M. Kishimoto, P.R. Shearing, S. Menkin, D. Golodnitsky, J. Gelb, E. Peled, N.P. Brandon, Three-dimensional high resolution X-ray imaging and quantification of lithium ion battery mesocarbon microbead anodes, J. Power Sources 248 (February) (2014) 1014–1020, http://dx.doi.org/10.1016/j.jpowsour.2013.08.147.

[38] L. Leu, S. Berg, F. Enzmann, R.T. Armstrong, M. Kersten, Fast X-ray micro-tomography of multiphase flow in berea sandstone: a sensitivity study on image processing, Transp. Porous Media 105 (September (2)) (2014) 451–469, http://dx.doi.org/10.1007/s11242-014-0378-4.

[39] T.L. Burnett, S. a McDonald, a Gholinia, R. Geurts, M. Janus, T. Slater, S.J. Haigh, C. Ornek, F. Almuaili, D.L. Engelberg, G.E. Thompson, P.J. Withers, Correlative tomography, Sci. Rep. 4 (January) (2014) 4711, http://dx.doi.org/10.1038/srep04711.

[40] J.M. Angelo, A. Cvetkovic, R. Gantier, A.M. Lenhoff, Characterization of cross-linked cellulosic ion-exchange adsorbents: 2. Protein sorption and transport, J. Chromatogr. A 1438 (2016) 100–112, http://dx.doi.org/10.1016/j.chroma.2016.02.019.

[41] B. Tjaden, J. Lane, T.P. Neville, L.D. Brown, T.J. Mason, C. Tan, M.M. Lounasvuori, D.J.L. Brett, P.R. Shearing, Comparison of ionic and diffusive mass transport resistance in porous structures, Electrochem. Soc. Trans. 75 (42) (2017) 135–145, http://dx.doi.org/10.1149/07542.0135ecst.

[42] G.M. Somfai, E. Tátrai, L. Laurik, B.E. Varga, V. Ölvedy, W.E. Smiddy, R. Tchitnga, A. Somogyi, D.C. Debuc, Fractal-based analysis of optical coherence tomography data to quantify retinal tissue damage, BMC Bioinf. (2014) 1–10, http://dx.doi.org/10.1186/1471-2105-15-295.